Editors' Suggestion

Kinematics of a simple reciprocal model swimmer at intermediate Reynolds numbers

Thomas Dombrowski[1] and Daphne Klotsa[2,*]

[1]*Department of Physics, University of North Carolina at Chapel Hill, Chapel Hill, North Carolina 27599, USA*

[2]*Department of Applied Physical Sciences, University of North Carolina at Chapel Hill, Chapel Hill, North Carolina 27599, USA*

(Received 6 February 2020; accepted 21 May 2020; published 24 June 2020)

We computationally studied the kinematics of a simple reciprocal model swimmer (asymmetric dumbbell) in a Newtonian fluid as a function of the Reynolds number (Re), and investigated how the onset and gradual increase of inertia impacts swimming behavior: a reversal in the swim direction, flow field, and the swim stroke. We divided the swim stroke into the increase and decrease in the distance between the two spheres (expansion and compression respectively) and related them to power and recovery strokes. We found that the switch in swim direction also corresponds to a switch in power and recovery strokes. We obtained expressions for the mean swimming velocity by collapsing the net displacement during expansion and compression under power-law relationships with respect to Re, the swimmer's amplitude, and the distance between the two spheres. Analyzing the fluid flows, we saw that the averaged flow field during expansion always resembles a pusher and during compression it always resembles a puller, but when averaged over the whole cycle, the flow that dominates is the one that occurs during the power stroke. We also related the power and recovery strokes to the swimming efficiency during times of expansion and compression, and found that the power stroke is, surprisingly, not always more efficient than the recovery stroke. Our results may have important implications in biology and ultimately the design of artificial swimmers.

DOI: 10.1103/PhysRevFluids.5.063103

I. INTRODUCTION

Biological and artificial swimmers exist across a broad range of length scales, from micron-sized bacteria and self-propelled nanoparticles to large aquatic organisms and marine robots on the order of meters. Swimming can be categorized by the Reynolds number (Re), which relates viscous and inertial forces. Microscopic swimmers at low Re, where viscosity dominates, swim differently from high-Re swimmers, where inertia dominates. Indeed, in nature one can see bacteria swim with a corkscrew chiral flagellum at low Re, while larger fish undulate their bodies pushing fluid backward to move forward at high Re. Between the two extremes resides the intermediate Reynolds regime (Re $\approx$ 0.1–1000), where both viscosity and inertia play a role. Mesoscopic organisms, i.e., those that operate at intermediate Re, are diverse both in size, $\approx$0.5 mm–50 cm, and in swimming mechanisms, including, for example, jet propulsion of squid and jellyfish [1,2], rowing of copepod antennae [3,4], aquatic flapping flight of pteropods [5,6], anguilliform (eel-like) locomotion [7–11], and ciliate beating [12,13]. Understanding motility in fluids is important both for answering fundamental biological questions, such as how do organisms swim, feed, communicate, etc., but also for the design of artificial swimmers and flyers, such as marine robots and drones.

*dklotsa@email.unc.edu

To gain insight into generic features and underlying physical mechanisms, simple theoretical models have been developed such as the scallop and Purcell's three-link swimmer [14], the squirmer model [15–18], asymmetric and symmetric dumbbell swimmers [19–21], the three-sphere swimmer [22], and the push-me-pull-you swimmer [23]. Most of the models have focused on microscopic scales where inertia is negligible, because (a) there are a lot of interesting biological questions and applications at microscopic scales, such as intracellular dynamics and processes in the cytoplasm, cell motility, bacteria, and algae [24], as well as artificial swimmers, such as self-propelled colloids and nanoparticles aspiring, for example, to aid in drug delivery [25,26]; and (b) Stokesian swimmers must break time reversibility, which makes their design theoretically challenging. While the Stokes regime is indeed very interesting, it is as important to understand what happens as we move away from the strict $\mathrm{Re} = 0$ Stokes regime, when and how inertia kicks in, and its consequences for different kinds of swimmers (e.g., different geometries and motility mechanisms). Models that include finite inertia are the inertial squirmer [27–33], the flapping plate [34,35], and the asymmetric and symmetric dumbbell swimmers [36–40].

It is worth noting that a lot of biology takes place near the boundary between the Stokes and intermediate Reynolds regimes, yet where the boundary is precisely is generally unknown. It matters where the boundary is because organisms have to change their swimming mode, feeding strategy, etc. depending on the regime in which they live. Switching regimes is not unusual; in fact, a plethora of organisms born into the Stokes regime move out of it as they grow in size. We would expect that they also change the way they move as a result of this change in regime. For example, the mollusk *C. antarctica* switches from using cilia to flapping as it grows [41], the brine shrimp transitions from rowing to gliding with metachronally beating legs [42], and the nymphal mayfly transitions from rowing to flapping with its gill plates [43]. From an applications point of view, understanding the physics near the boundary can help us design artificial swimmers or (microfluidic) processes that utilize the relative ratio of inertial and viscous forces, switching between regimes, and thus switching between desired properties. For a longer discussion on the motivation and importance of studying motility at intermediate Re, including applications in biology and materials, see this perspective article [44].

In this paper, we studied the kinematics of a simple reciprocal model swimmer as a function of the Reynolds number. The same asymmetric dumbbell model (termed the spherobot) was determined to switch swim direction depending on the Reynolds number because of the corresponding induced steady streaming flows [39]. The spherobot switched from a small-sphere-leading regime to a large-sphere-leading regime at $\mathrm{Re}_c \approx 20$. Here, we studied the motion of the spherobot swimmer in more detail by splitting its oscillation into the expansion and compression of the two spheres, and we collapsed their corresponding net displacements under piecewise power-law relationships with respect to Re, inverse Strouhal number ϵ, and equilibrium distance between spheres d_0. We also related the expansion and compression to power and recovery strokes. We found that the switch in swim direction as Re increased corresponded to a switch in the power and recovery strokes. In the small-sphere leading regime ($\mathrm{Re} < \mathrm{Re}_c$), the power stroke occurred during compression and the recovery stroke occurred during expansion, while the reverse occurred in the large-sphere-leading regime ($\mathrm{Re} > \mathrm{Re}_c$). We noticed how as Re increased and inertial forces became more dominant, our swimmer transitioned from a jerky, back-and-forth motion with a large backward displacement during the recovery stroke in the small-sphere-leading regime to a continuous movement forward in the direction of swimming all in the same direction, with no backward displacement during the recovery stroke in the large-sphere-leading regime. By studying the fluid flows, we saw that the averaged flow field during expansion was always pusherlike and during compression it was pullerlike, which is to be expected, but when averaged over the whole cycle one of the two flow fields dominated. We determined that the most dominant flows consistently occurred during the power stroke in each regime. We also related the power and recovery strokes to the spherobot's efficiency during times of expansion and compression, and we found that the power stroke was, surprisingly, not always more efficient than the recovery stroke. The subtle differences in Re that

(a)

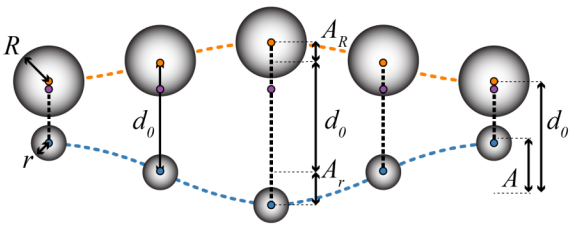

(b) Simulation specs and parameters

Specifications	Value
Eulerian grid dimensions (m/r)	53.3×53.3
number of Eulerian grid levels	4
Eulerian grid refinement ratio	1:4
effective Eulerian grid resolution	512×512
time step size, Δt (s)	10^{-4}
Parameters	
Reynolds number, Re	$[10^{-3}, 150.0]$
sphere radii ratio, $\alpha = R/r$	2
amplitude, $\epsilon = A/r$	[0.8, 1.6]
frequency, f (s^{-1})	10
$M = r\sqrt{\omega/\nu} = r/\delta$	[0.88, 11.89]
equilibrium distance, $\hat{d}_0 = d_0/r$	[5.0, 10.0]

FIG. 1. (a) Reciprocal oscillation of the spherobot swimmer over one cycle. The large sphere (orange) with radius R always oscillates in the opposite direction of the small sphere (blue) with radius r. The distance between the spheres $d(t) = d_0 + A\sin(2\pi ft)$ is prescribed to be of a simple harmonic oscillator with frequency f, where d_0 is the equilibrium distance between the spheres, and $A = A_r + A_R$ is the amplitude of the spherobot. The amplitudes of the small and large spheres are A_r and A_R, respectively. When absent of fluid, the spherobot's center of mass (CM), shown in purple, does not move throughout the oscillation. (b) Simulation specifications and parameters.

can lead to switching regimes and swim strokes may have important implications for biology and ultimately the design of artificial swimmers.

The structure of the paper is as follows. In Sec. II we briefly describe the model, the computational method, and simulation details. In Sec. III we present results for the kinematics of the spherobot, and in Sec. IV we present results for averaged fluid flows, efficiencies, and the evolution of fluid flow. We end with a discussion and conclusions in Sec. V.

II. MODEL, METHODS, AND BACKGROUND

The spherobot is a geometrically simple, reciprocal model swimmer composed of two unequally sized spheres of radii R and r, such that $R > r$ (asymmetric dumbbell); see Fig. 1(a) and Refs. [39,45]. The spheres oscillate in antiphase with respect to each other, and they are coupled to one another by prescribing the distance between their centers, $d(t) = d_0 + A\sin(2\pi ft)$, with an actuated spring, where d_0 is the equilibrium distance between the centers, A is the amplitude of the spherobot, $A = 0.5(d_{\max} - d_{\min})$, and f is the frequency of oscillation; see Fig. 1(a). At each time step, the equilibrium distance of the actuated spring is updated, and an equal and opposite force is applied to each sphere to move them a desired distance, $d(t)$, apart. The magnitude and direction of the force applied to each sphere depend on the relative positions of the two spheres. $[F_R(t), F_r(t)] = [+, -]k[d(t) - x(t)]$, in which F_R is the force applied to the large sphere, F_r is the force applied to the small sphere, k is a spring constant, and $x(t)$ is the current (actual) distance between the spheres. Note that $F_R = -F_r$ at every instance in time (i.e., the swimmer is self-propelled). The prescribed distance between the spheres' centers changes sinusoidally with time, and the model ensures a geometrically reciprocal cycle (error $\approx 1/1000$th of the small spheres radius). The model conditions ensure that the spherobot swims only along the oscillation axis (vertical). Since the forces were equal in magnitude and the spheres were of the same density, their amplitudes were different: $A_R < A_r$ and $A = A_R + A_r$. Subscripts R and r indicate quantities specific to the large and small sphere, respectively. Both spheres were neutrally buoyant with the surrounding fluid, i.e., they had equal densities $\rho_p = \rho_f = \rho$.

The spherobot was immersed in a viscous, incompressible Newtonian fluid that occupied a finite cell with no-slip walls. The fully coupled fluid-structure interaction system was resolved using the constrained immersed boundary (CIB) method [46,47]. The CIB scheme was implemented in

IBAMR, which is an immersed boundary numerical method with adaptive mesh refinement [48,49]. The IB method for fluid-structure interaction uses an Eulerian formulation of the momentum equation and incompressibility constraint for the coupled fluid-solid system along with a Lagrangian description of the motion of the immersed structures. Let $\mathbf{x} \in \Omega$ be fixed Eulerian physical coordinates, and let $\mathbf{s} \in U^i$ be fixed Lagrangian curvilinear coordinates attached to the structure. In our notation, $\mathbf{X}(\mathbf{s}, t) \subset \Omega$ is the physical position of material point $\mathbf{s}$ at time t. The momentum equation and incompressibility constraint are given by

$$\rho \frac{D\mathbf{u}}{Dt}(\mathbf{x}, t) = -\nabla p(\mathbf{x}, t) + \mu \nabla^2 \mathbf{u}(\mathbf{x}, t) + \mathbf{f}(\mathbf{x}, t), \tag{1}$$

$$\nabla \cdot \mathbf{u}(\mathbf{x}, t) = \mathbf{0}, \tag{2}$$

in which $\mathbf{u}(\mathbf{x}, t)$ is the material velocity field, $p(\mathbf{x}, t)$ is the pressure field that imposes the incompressibility constraint, $\mathbf{f}(\mathbf{x}, t)$ is a body force that arises from the presence of the immersed structure, ρ is the mass density, and μ is the viscosity. Eulerian and Lagrangian variables are coupled via integral transforms with Dirac delta function kernels:

$$\mathbf{f}(\mathbf{x}, t) = \int_U \mathbf{F}(\mathbf{s}, t) \delta(\mathbf{x} - \mathbf{X}(\mathbf{s}, t)) d\mathbf{s}, \tag{3}$$

$$\mathbf{U}(\mathbf{s}, t) = \int_\Omega \mathbf{u}(\mathbf{x}, t) \delta(\mathbf{x} - \mathbf{X}(\mathbf{s}, t)) d\mathbf{x}. \tag{4}$$

Equation (3) converts the Lagrangian force density $\mathbf{F}(\mathbf{s}, t)$ (which is a Lagrange multiplier force that constrains the spheres to move as rigid bodies) to an equivalent Eulerian force density $\mathbf{f}(\mathbf{x}, t)$, and Eq. (4) evaluates the local material velocity at each structural position.

The position of each sphere of the spherobot is updated via

$$\frac{\partial \mathbf{X}}{\partial t}(\mathbf{s}, t) = \mathbf{U}(\mathbf{s}, t) = \mathbf{V}_{\mathrm{COM}} + \mathbf{W}_{\mathrm{COM}} \wedge \mathbf{R}(\mathbf{s}, t), \tag{5}$$

in which $\mathbf{V}_{\mathrm{COM}}$ and $\mathbf{W}_{\mathrm{COM}}$ are the (unknown) translational and rotational velocities, respectively, and $\mathbf{R}(\mathbf{s}, t) = \mathbf{X}(\mathbf{s}, t) - \mathbf{X}_{\mathrm{COM}}(t)$ is the radius vector to the center of mass of the sphere. The Lagrangian force density $\mathbf{F}(\mathbf{s}, t)$ is required to satisfy the net external force and torque constraint on the immersed body:

$$\int_U \mathbf{F}(\mathbf{s}, t)\, d\mathbf{s} = \mathbf{F}_{\mathrm{external}}, \tag{6}$$

$$\int_U \mathbf{R}(\mathbf{s}, t) \wedge \mathbf{F}(\mathbf{s}, t)\, d\mathbf{s} = \mathbf{T}_{\mathrm{external}}. \tag{7}$$

We remark that the net external force and torque on the immersed structure excludes hydrodynamic traction forces on the surface of the body, but could include forces and torques arising, for example, due to gravity, surface tension, tethered springs, etc. In the case of the spherobot, $\mathbf{F}_{\mathrm{external}}$ is nonzero and results from the force applied by the actuated spring, and $\mathbf{T}_{\mathrm{external}} =$ because the actuated spring passes through the centers of masses of the two spheres. There are no other external forces or torques.

In our computer model, each sphere of the spherobot was composed of a mesh of Lagrangian marker points that were generated using an in-house Python code, and the singular δ-function kernels were replaced by a six-point regularized kernel function [46]. The remainder of the spatial discretization and the time stepping algorithm for the CIB method have been described in detail in prior work [46,47].

An adaptive mesh was implemented to improve the efficiency of the simulation. The coarsest level was broken up into $N = 8$ cells along one dimension. We used a grid refinement ratio of 1 : 4 where the next highest refinements are $N = 32$, 128, and 512. There were four refinement levels,

and the spherobot's mesh was evaluated at the highest grid refinement of $N = 512$. The simulation box was $6\times$ the length of the swimmer and it was $53\times$ the radius of the small sphere to prevent interactions with the wall.

In previous work, we investigated the spherobot, which was shown to switch swim direction depending on a critical Re [39]. The swim direction was related to the reversal of steady streaming flows (SS) around the small sphere [50]. We note three important findings that are relevant in this paper too: (i) The steady streaming reversal of the time-averaged flow fields over a cycle is qualitatively similar to puller and pusher flow fields defined in Stokes flows, although our swimmers were at finite inertia and no assumptions were made on the fluid flows; (ii) we showed that steady streaming flows can be used as a propulsion mechanism, which is especially interesting in the low-intermediate Re < 20, where inertia is weak; and (iii) Although the SS flows reversal is gradual as a function of Re, the result in a system like ours is a drastic change in behavior, namely a switch in the direction of swimming.

Before further discussion of the spherobot, let us first consider the simpler problem of a single oscillating sphere with angular frequency ω, amplitude A, and radius r. As discussed in Ref. [27], in general there are three relevant dimensionless ratios in this class of problems: the frequency (flapping) Reynolds number $\mathrm{Re}_f = rA\omega/\nu$, which scales with the nonlinear advective term in the Navier-Stokes equations [27,51–53]; $M^2 = r^2\omega/\nu$, which scales with the unsteady term in the Navier-Stokes equations [50]; and the particle Reynolds number $\mathrm{Re}_p = \rho_p r^2\omega/\rho_f\nu$, which quantifies the particle inertia. Note that for us $\rho_p = \rho_f$ so the particle Reynolds number reduces to M^2. The oscillatory motion introduces a relevant length scale, the oscillatory boundary layer thickness, $\delta = \sqrt{\nu/\omega}$ [54]. M can also be thought of as the ratio of the particle radius r to the oscillatory boundary layer thickness δ. An oscillating sphere also produces a nonzero cycle-averaged flow otherwise known as steady streaming, and there is an additional dimensionless ratio, the streaming Reynolds number $\mathrm{Re}_s = A^2\omega/\nu$, which quantifies the steady streaming flows around a single oscillating sphere beyond the oscillatory boundary layer [50,55,56]. At intermediate Reynolds numbers, choosing which dimensionless ratio best characterizes the system is challenging because a lot of the parameters can have similar magnitudes, as is the case here. Thus, even for the simpler case of one oscillating sphere, there are at least four relevant dimensionless ratios.

Additional complexity enters the system when we include a second sphere of a different size oscillating antiphase, resulting in net motion, i.e., swimming. First, there are the extra length scales the second sphere introduces, e.g., the radius and amplitude of the second sphere, and the distance between spheres. Second, there is a swimming Reynolds $\mathrm{Re}_{\mathrm{swim}} = Ul/\nu$, where U is the swim velocity and l is the swimmer's length scale. It is worth noting that for experimentally relevant systems, many of these length scales (that enter the different dimensionless ratios) are of the same order of magnitude giving values for the ratios close to 1. As a result, the problem becomes more challenging and often analytically intractable [57].

Here, we use $\mathrm{Re} = A_r r\omega/\nu$ as the reference Reynolds number (for simplicity, the notation will be just Re) because that was the Re we found to determine the spherobot switch in the swim direction from a small-sphere-leading regime (SSL) to a large-sphere-leading regime (LSL) in previous work [39]. Note that a similar Re has been shown to dominate other intermediate-Re phenomena: the scaling of the stagnation point indicating the reversal of outer and inner steady streaming [58,59] and the gap between two granular spheres oscillating in phase [60,61].

We investigated the spherobot's movement in Stokes flow and in the range of $0.1 \leqslant \mathrm{Re} \leqslant 150$. To give some intuition to the reader, if we were to observe a dumbbell composed of a small sphere with radius $r = 1$ mm and a large sphere with radius $R = 2r = 2$ mm that swims in water and oscillates with a frequency $f = 10$ Hz and amplitude $A = r = 1$ mm, the Reynolds number would be in the intermediate range, $\mathrm{Re} = 2\pi f A_r r/\nu = 50.3$. We defined the length scales with respect to the radius of the small sphere r and the time scales with respect to the frequency of the oscillation f. We introduced the dimensionless positions, velocities, equilibrium distance between spheres, and

TABLE I. List of net displacements.

Variable	Definition
$\Delta\hat{y}_{\mathrm{CM}}$	center of mass
$\Delta\hat{y}_R$	large sphere
$\Delta\hat{y}_r$	small sphere
$\Delta\hat{y}_{\mathrm{exp}}$	expansion
$\Delta\hat{y}_{\mathrm{com}}$	compression
$\Delta\hat{y}_{\mathrm{min}}$	shift in compression
$\Delta\hat{y}_+$	along $\langle\hat{v}_{\mathrm{CM}}\rangle$
$\Delta\hat{y}_-$	opposite to $\langle\hat{v}_{\mathrm{CM}}\rangle$

time,

$$\hat{y} = y/r, \quad \hat{v} = v/fr, \quad \hat{d}_0 = d_0/r, \quad \tau = ft, \tag{8}$$

as well as the amplitude, kinematic viscosity, and large sphere radius,

$$\epsilon = A/r, \quad M = r\sqrt{\omega/\nu} = r/\delta, \quad \alpha = R/r, \tag{9}$$

in terms of their dimensional counterparts. We performed a parameter sweep varying the fluid's kinematic viscosity M, the spherobot's amplitude ϵ, and the equilibrium distance between spheres $\hat{d}_0$, while keeping the spheres' radii R and r, frequency f, and sphere and fluid density ρ constant ($\alpha = R/r = 2$ and $\rho = 2$ kg/m^3). All of the simulation parameters are shown in Fig. 1(b). The simulations were run long enough for the spherobot to reach a steady state, defined as less than a 1% change in the average velocity over consecutive oscillations. Data were acquired after steady state was reached. In most of the paper we focused on two characteristic systems, one in the small-sphere-leading regime at Re $= 2.5$ and one in the large-sphere-leading regime at Re $= 70.0$. For both systems, $\hat{d}_0 = 6.5$ and $\epsilon = 1.2$. We used the software VISIT [62] for fluid flow analysis. Other analysis was done using in-house PYTHON code. In the rest of the paper, we assume the spherobot is placed vertically (y-direction) with the large sphere on top and the small sphere at the bottom (as shown in Fig. 1). For all figures showing a characteristic cycle of oscillation, the data are shifted in the time axis in the following way. The first half of the cycle is a region of expansion, followed by a region of compression in the second half. We define $\tau = ft$ as our dimensionless time unit, essentially the fraction of time elapsed in the cycle. At $\tau = 0.00, 1.00$ the spheres are at minimum distance $\hat{d}_0 - \epsilon$, at $\tau = 0.50$ they are at maximum distance $\hat{d}_0 + \epsilon$, and at $\tau = 0.25, 0.75$ they are at their equilibrium distance apart $\hat{d}_0$. We used a number of variables to describe the net displacement of the spherobot during its cycle, as shown in Table I.

III. RESULTS

A. Kinematics

We first studied how the periodic oscillation of the two spheres that composed the spherobot resulted in net displacement of their combined center of mass (CM) over one cycle, $\hat{y}_{\mathrm{CM}} = (\hat{y}_r m_r + \hat{y}_R m_R)/(m_r + m_R)$, where $\hat{y}$ indicates the position along the swimmer's axis and m is the mass of each sphere indicated by the subscript, for a range of Re (Fig. 2). Note that because of the unequal masses of the spheres, the CM is actually on the large sphere (see Fig. 1) and as such closely follows the trajectory of the large sphere. We used the CM to indicate the displacement and velocity of the spherobot as a whole. Moreover, displacement was measured in relation to the position of the CM at the start of the cycle at $\hat{y}_{\mathrm{CM}} = 0$. The full parameter range of data shown in Table I is found in the supplemental information (SI). We present our findings where the spherobot's amplitude, $\epsilon = 1.2$, the equilibrium distance between spheres, $\hat{d}_0 = 6.5$, and the individual sphere radii, $\alpha = 2$, were

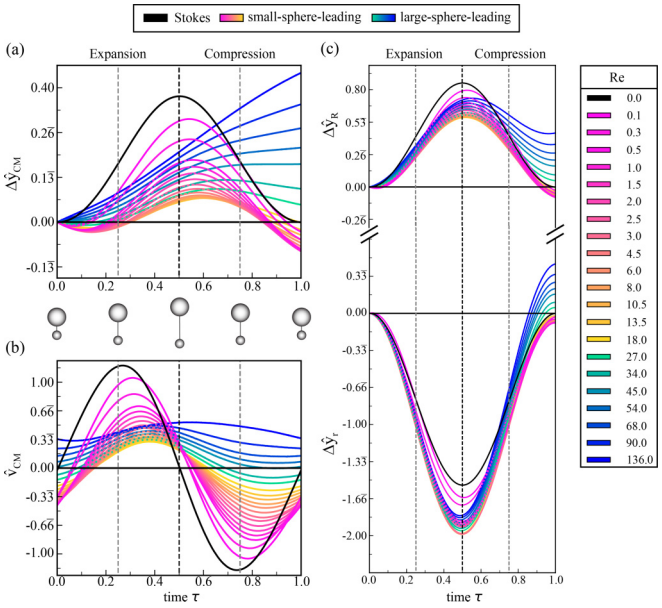

FIG. 2. Kinematic quantities plotted as functions of time over one cycle of oscillation after steady state had been reached. (a) Displacement of spherobot, represented by the net displacement of its center of mass $\Delta\hat{y}_{\mathrm{CM}}$, (b) velocity of spherobot represented by $\hat{v}_{\mathrm{CM}}$, and (c) displacement of individual spheres of radius R and r. Net swimming direction is indicated by the colors of the curves (black, Stokes flow; pink to yellow, small-sphere-leading; and green to blue, large-sphere-leading). The Reynolds number is represented by the shading of the curves; see the legend.

held constant such that Re was only $\propto 1/\nu$. In other words, Re was increased gradually via the kinematic viscosity ν.

For Re $= 0$ (Stokes flow), the spherobot's reciprocal motion resulted in no net displacement over a cycle, as expected from the scallop theorem [14]. It moved in the direction of the large sphere during expansion, reaching maximum displacement halfway through the cycle, and then it moved in the direction of the small sphere during compression, ultimately returning exactly where it began; see Fig. 2(a), black curve.

1. Small-sphere-leading

As we transitioned from Stokes flow to intermediate Re, the spherobot's trajectory changed; see Fig. 2(a), pink to yellow curves. At the start of its cycle, the spherobot moves forward (small sphere on the front), then slightly in the opposite direction during expansion and the initial part of compression; it moves with the small sphere on the front for the rest of the compression, with net displacement in that same direction at the end of the cycle. Note that the maximum displacement during the cycle is in the opposite direction to that of net swimming. This backward maximum displacement occurred at the half-period mark for Stokes flows and was shifted to a later time $\tau \approx 0.55$–0.65 in the small-sphere-leading (SSL) regime. As Re increased both the maximum backward displacement near the half-period mark and the net displacement at the end of the cycle got smaller, see curves from Re $= 0.5$ to 13.5, at $\tau \approx 0.5$ and $\tau = 1$, respectively. For Re $= 18.0$, the net displacement after one cycle is ≈ 0. The spherobot will switch direction and transition from the small-sphere-leading to the large-sphere-leading regime.

2. Large-sphere-leading

In the large-sphere-leading (LSL) regime we see two behaviors; see Fig. 2(a), green to blue curves. First, for Re = 27 and 34, at the start of its cycle, the spherobot moves backward slightly (small sphere on the front), and then moves forward (large sphere on the front) during expansion. It then continues to move forward during compression, only to slightly move back again at the end of the compression, with net displacement toward the large sphere. Already, it is clear that in the large-sphere-leading regime, the spherobot is hardly ever found to be with displacement in the opposite direction to its swimming, contrary to the small-sphere-leading regime. Then, as Re increases further (Re $>$ 45), the backward motion is suppressed more until the spherobot moves in the direction of swimming at all times. The two behaviors are more evident from the velocity plots [see Fig. 2(b), green curves], where for Re = 27 and 34 the velocity at the start and the end of the cycle is negative (toward the small sphere), while for all other higher Re the velocity is always positive (toward the large sphere).

3. Separate spheres

To understand how each sphere contributes to the overall motion, we also looked at the kinematics of the spheres separately; see Fig. 2(c). During expansion, for both regimes the large sphere's net displacement is always LSL, and the small sphere's is Rr always SSL. During compression, the large and small spheres do the opposite, i.e., the large sphere's net displacement Dy_R is always SSL, and the small sphere's Dy_r is always LSL. The distinction in the trajectories of the two regimes seems to appear during compression.

In Stokes flow, the trajectory of each sphere is symmetric with respect to time over a cycle, and the two spheres are always antiphase. As we increase Re, the individual spheres are affected by the onset of inertia differently, resulting in a phase difference between them. We present data for two characteristic systems (described in Sec. II), one in each regime. In Fig. 3, we compared the velocities of the large sphere (orange), small sphere (blue), CM (purple), and identified regions of "slip" to be when both spheres moved in the same direction. When both spheres' velocities are negative (toward the small sphere), we call this SSL-slip, and when they are both positive (toward the large sphere), we call it LSL-slip. In the small-sphere-leading regime, at the end of expansion and the start of compression we found slip in the direction opposite to swimming (LSL-slip), while at the end of compression and the start of expansion we found a larger slip in the direction of swimming (SSL-slip); see Fig. 3(a). In the large-sphere-leading regime, at the end of expansion and the start of compression the slip was still LSL but now in the direction of swimming, while at the end of compression and the start of expansion we found that the direction of slip depended on the Re. As Re increased, the slip switched to LSL. In other words, the increase in inertia only affected the slip direction after compression. So, we identified for Re $>$ 0.0 two contributions to the motion of the spherobot, namely the oscillatory and the slip (steady).

We also varied ϵ and $\hat{d}_0$ in addition to ν, shown in Fig. 2. The full parameter range is shown in Table I, and additional plots are included in the SI (Sec. I). The magnitude of the net displacement at the end of the cycle increased when ϵ and Re also increased. Conversely, the net displacement decreased when $\hat{d}_0$ increased (Figs. S1 and S2 of the SI).

To help identify trends in the data, we decomposed $\Delta\hat{y}_{\mathrm{CM}}$ into the net displacements during expansion $\Delta\hat{y}_{\mathrm{exp}}$ and during compression $\Delta\hat{y}_{\mathrm{com}}$. Figures 4(a) and 4(b) show an example of this decomposition for all amplitudes and equilibrium distances studied. Let us consider expansion first. When the $\Delta\hat{y}_{\mathrm{exp}}$ data are plotted on a log-log scale, see Fig. 4(a), we see a constant negative slope followed by a constant positive slope, indicative of two regions, each defined by a power law in Re. If we now consider compression and look at the data for $\Delta\hat{y}_{\mathrm{com}}$ on a log-log scale, see Fig. 4(b), we observe three distinct trends with respect to Re all with positive slopes, also determined to be power laws with different exponents. We considered three variables Re, $\epsilon = A/r$, and $\hat{d}_0$ and assumed they are independent of one another. We partitioned the data into two expansion regions and three compression regions with Re, and we performed a multiple variable linear regression on each. It is

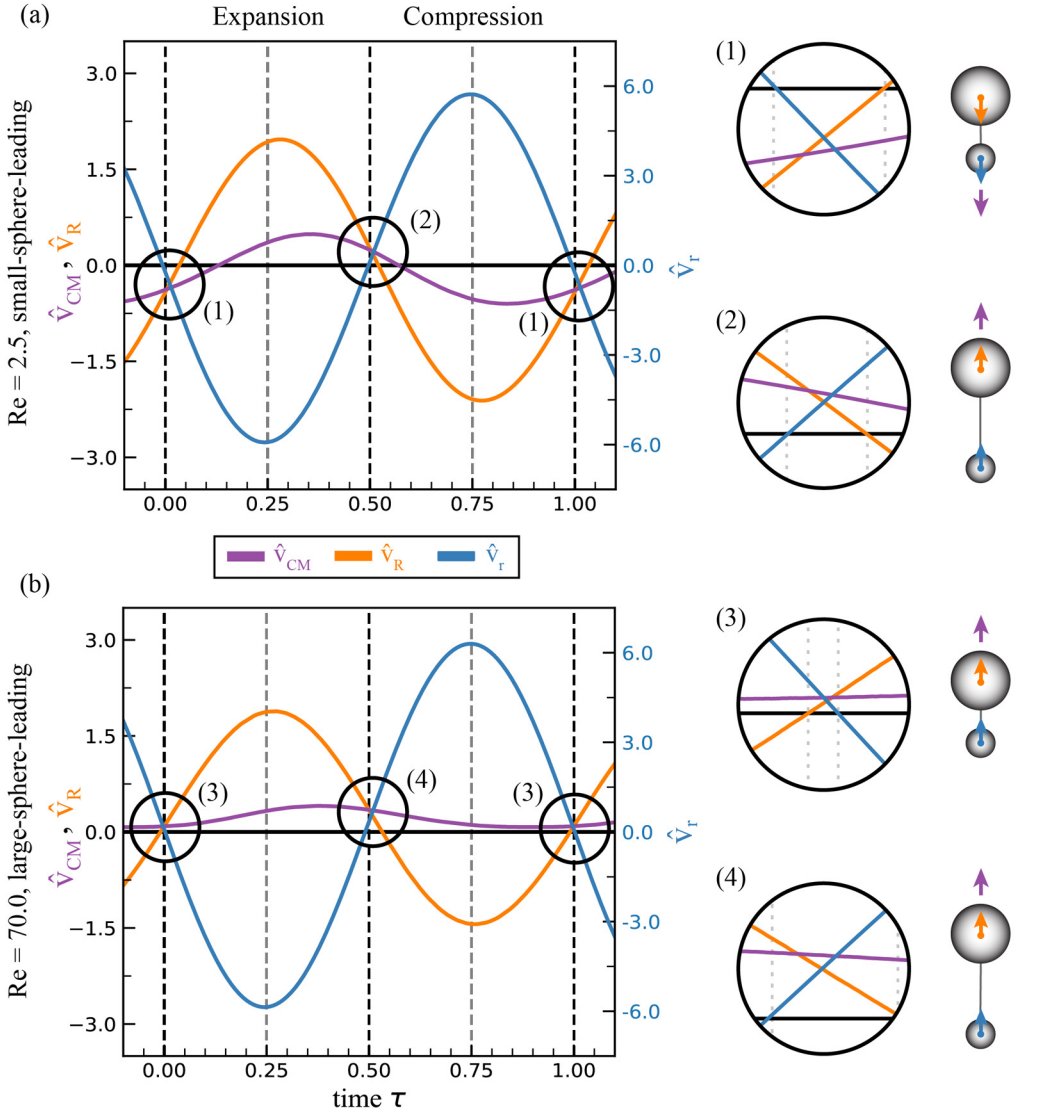

FIG. 3. We define slip to be the region of movement where both spheres move in the same direction. As a result, the entire spherobot moves in the same direction as its spheres. Here, we show the nondimensional velocities (v/fr) of the spherobot $\hat{v}_{\mathrm{CM}}$ (purple), its large sphere $\hat{v}_R$ (orange), and its small sphere $\hat{v}_r$ (blue) when it is (a) small-sphere-leading and (b) large-sphere-leading. We identify the regions of slip observed during each spherobot's oscillation with black circles, and the region is magnified to the right. For the (a) small-sphere-leading spherobot, slip regions (1) and (2) are shown. Region (1) displays a region where slip is small-sphere-leading. It occurs at the end of compression and at the start of expansion. Region (2) shows a region where slip is large-sphere-leading. It occurs at the end of expansion and the start of compression. For the (b) large-sphere-leading spherobot, slip regions (3) and (4) are identified. Regions (3) and (4) show regions where the spherobot slips large-sphere-leading. Region (3) occurs at the end of compression and the start of expansion. Region (4) occurs at the end of expansion and the start of compression.

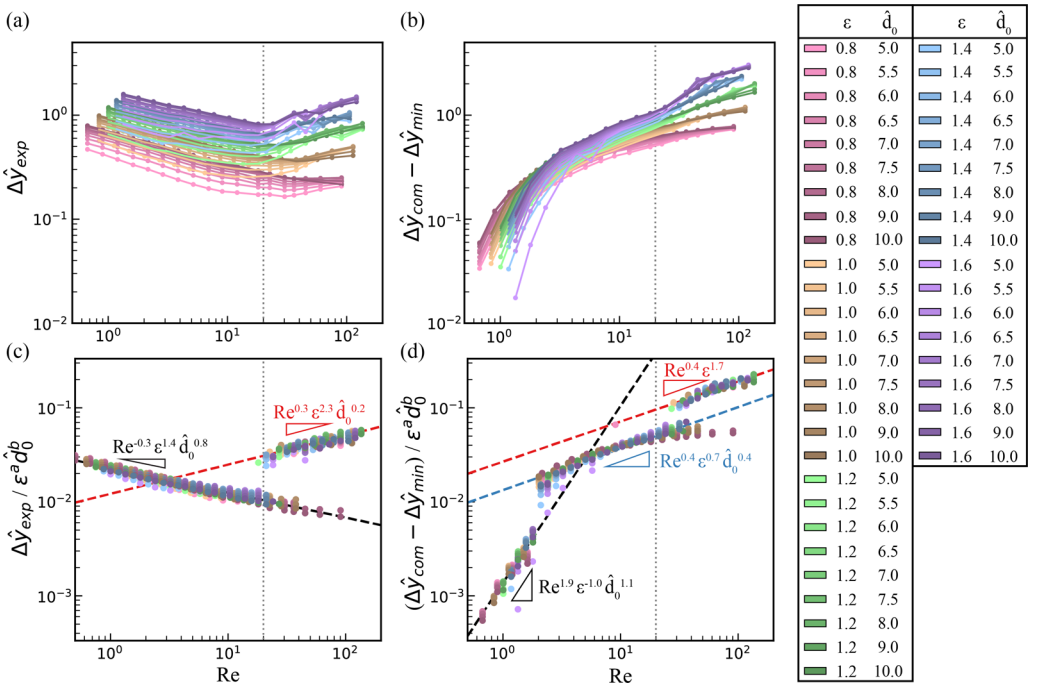

FIG. 4. (a) Net displacement of the spherobot during expansion $\Delta\hat{y}_{\text{exp}}$ as a function of Re on a log-log scale for all ϵ and $\hat{d}_0$ simulated; see the legend. Curves show a constant negative slope followed by a positive slope except for when both $\epsilon = 0.8$ (pink) and $\hat{d}_0 = 9.0, 10.0$. The turning point and the positive slope change for different amplitudes ϵ (color). (b) Net displacement of the spherobot during compression $\Delta\hat{y}_{\text{com}}$ as a function of Re on a log-log scale. There are three distinct positive slope trends with Re. We fit the expansion and compression displacements with respect to Re, ϵ, and d_0 using a multiple variable linear regression. (c) $\Delta\hat{y}_{\text{exp}}$ vs Re on a log-log scale collapsed into a negative slope (black dashed) and a positive slope region (red dashed). (d) $\Delta\hat{y}_{\text{com}}$ vs Re on a log-log scale collapsed into three distinct positive slope regions. The corresponding relationships with Re, ϵ, and d_0 are also shown in (c) and (d). The dotted gray line represents the critical Reynolds number where the swimming direction switches from small-sphere-leading to large-sphere-leading.

important to note that each region has a different dependence on Re, ϵ, and $\hat{d}_0$. For the expansion, the data were split where there was a minimum in $\Delta\hat{y}_{\text{exp}}$; see Fig. 4(a). For compression, the data were split where the slope changed at Re ≈ 2.0 and then again when $\Delta\hat{y}_{\text{exp}}$ was at a minimum (the same criterion as the expansion data); see Fig. 4(b). The resulting collapse is shown on a log-log scale in Figs. 4(c) and 4(d). Equations (10) and (11) show the fits for $\Delta\hat{y}_{\text{exp}}$ and $\Delta\hat{y}_{\text{com}}$, respectively, and their power-law relationships with Re, ϵ, and $\hat{d}_0$. It is worth noting that while there is currently no analytical theory for finite amplitudes, the expressions we obtained from the collapse can be used to give a prediction for the velocity of the spherobot, $\langle\hat{v}_{\text{CM}}\rangle = f(\Delta\hat{y}_{\text{exp}} + \Delta\hat{y}_{\text{com}})$, where f is the frequency of its oscillation,

$$\Delta\hat{y}_{\text{exp}} = \begin{cases} 10^{-1.6}\text{Re}^{-0.3}\epsilon^{1.4}\hat{d}_0^{0.8} & \text{Fig. 4(c) black,} \\ 10^{-1.9}\text{Re}^{0.3}\epsilon^{2.3}\hat{d}_0^{0.2} & \text{Fig. 4(c) red;} \end{cases} \tag{10}$$

$$\Delta\hat{y}_{\text{com}} = \begin{cases} 10^{-2.9}\text{Re}^{1.9}\epsilon^{-1.0}\hat{d}_0^{1.1} & \text{Fig. 4(c) black,} \\ 10^{-1.9}\text{Re}^{0.4}\epsilon^{0.7}\hat{d}_0^{0.4} & \text{Fig. 4(c) blue,} \\ 10^{-1.6}\text{Re}^{0.4}\epsilon^{1.7} & \text{Fig. 4(c) red.} \end{cases} \tag{11}$$

B. Power and recovery

To gain insight into the spherobot's motility mechanism in the two regimes, we divided its periodic motion into power and recovery strokes, a classical analysis for the motility of Stokesian swimmers [63]. In living organisms, a common way to define power and recovery strokes is as follows. The power stroke occurs when the swimmer's appendage, i.e., the part of the swimmer that generates motion, moves opposite to the direction of the mean swim velocity $\langle \hat{v}_{\mathrm{CM}} \rangle$, and the recovery stroke occurs when the appendage moves in the same direction as $\langle \hat{v}_{\mathrm{CM}} \rangle$ [64,65]. For example, one can imagine a human swimmer's breast stroke. The power stroke occurs when the swimmer's arms move back to propel the swimmer forward, and the recovery stroke occurs as the arms return to their original position. During the recovery stroke, the swimmer either moves backward or slows down depending on the motility mechanism, Re, etc. It is also important to note that organisms with reciprocal strokes (stroke the same forward in time as backward) cannot swim in Stokes flow, meaning the power stroke is identical to the recovery stroke, and the swimmer moves back and forth the same amount, e.g., the scallop or the spherobot.

How does a power and recovery stroke emerge as Re increases from 0 to finite? And how do the notions of power and recovery strokes evolve as Re increases further? We aim to answer these questions for the spherobot. We view the large sphere as the body of the swimmer and the small sphere as its appendage. The justification for this is that the small sphere moves the most as it has a larger amplitude than the large sphere; see also [39]. Thus, we define the power stroke to be when the velocity of the small sphere and the average velocity of the CM over the whole cycle are in opposite directions, $\hat{v}_r \langle \hat{v}_{\mathrm{CM}} \rangle < 0$, and the recovery stroke when the velocity of the small sphere and the average velocity of the CM are in the same direction, $\hat{v}_r \langle \hat{v}_{\mathrm{CM}} \rangle > 0$. Note that $\langle \hat{v}_{\mathrm{CM}} \rangle < 0$ in the small-sphere-leading regime and $\langle \hat{v}_{\mathrm{CM}} \rangle > 0$ in the large-sphere-leading regime.

In Fig. 5, we plot $\hat{v}_{\mathrm{CM}}$ (purple), with the displacements in the same direction as $\langle \hat{v}_{\mathrm{CM}} \rangle$ termed $\Delta\hat{y}_+$ (green area) and opposite to it $\Delta\hat{y}_-$ (red area), and we indicate power (P) and recovery strokes (R) in each regime. For $\mathrm{Re} = 0.0$, there was no distinction between power and recovery strokes because the spherobot does not swim, $\langle \hat{v}_{\mathrm{CM}} \rangle = 0.0$; see Fig. 5(a). Connecting to the two regimes, in the small-sphere-leading regime, Fig. 5(b), the spherobot performs a power stroke during compression and a recovery stroke during expansion. The effect of inertia is already apparent: the curve has shifted in the time axis compared to Stokes flow, such that, early in the recovery stroke, the swimmer is still moving forward due to the power stroke. Similarly, the swimmer is still moving backward early in the power stroke. As Re increases, the power and recovery strokes produce smaller displacements in both directions; see Fig. 5(c). As a result, the spherobot experiences less intense back-and-forth motion. Note that we do not see a further shift with respect to time. At the critical value where the transition in the swimming direction occurs ($\mathrm{Re} = 18.0$), expansion and compression generate smaller but equal displacements in both directions, so the spherobot remains stationary over a cycle; see Fig. 5(d). As Re increases further, the spherobot switches direction to swim large-sphere-leading, and now performs a power stroke during expansion and a recovery stroke during compression; see Figs. 5(e) and 5(f). Its periodic motion is still prescribed and does not change, but the power and recovery strokes reverse. There is also a behavioral change in the recovery stroke. When $\mathrm{Re} > 18$ but still close to the transition, the recovery stroke produces a backward displacement [Fig. 5(e)], while for higher Re the recovery stroke does not produce a backward displacement and just slows down the swimmer [Fig. 5(f)]. The power stroke, on the other hand, does not change much with Re, and the maximum velocity remains approximately constant. This is a demonstration showing how the movement of a simple model swimmer is affected by the onset and gradual increase of inertia.

IV. FLUID FLOWS AND EFFICIENCY

We showed that in the small-sphere-leading regime, the averaged flow over a cycle is pullerlike, i.e., the flow is pulled in toward the spheres along the swimming direction and is pushed out along

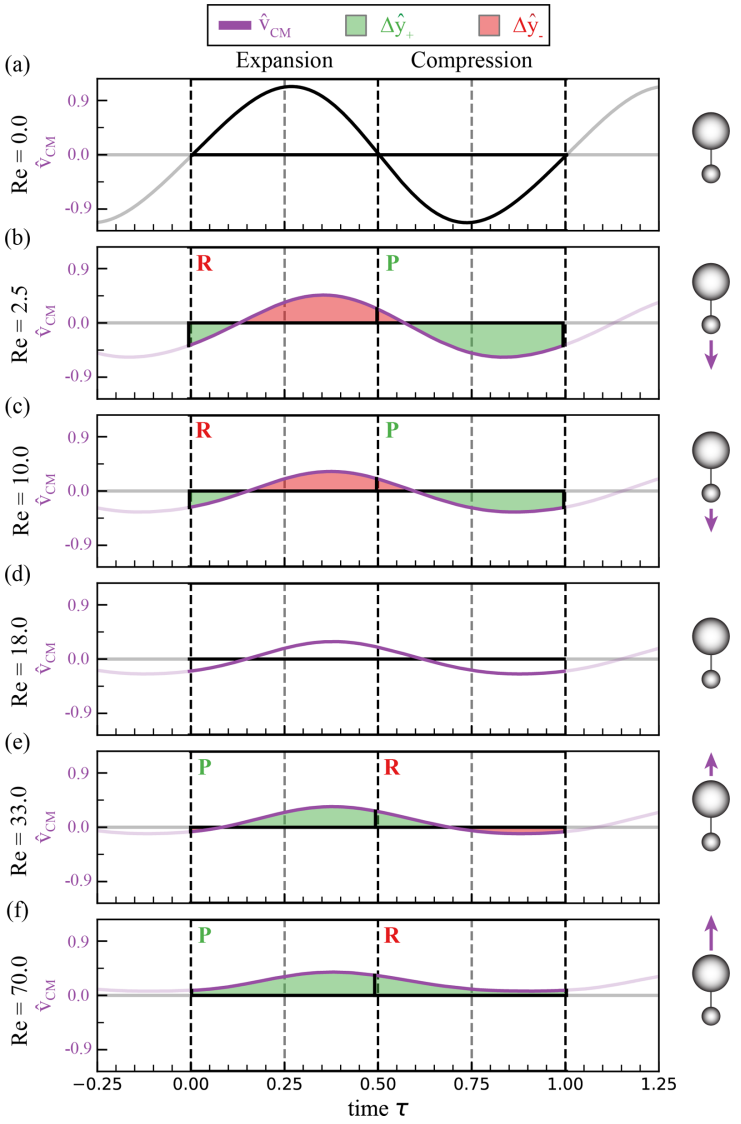

FIG. 5. The power and recovery stroke of the spherobot is determined by the movement of its appendage, the small sphere, represented by $\hat{v}_r$. We define the power stroke to be when the small sphere moves opposite to the direction of net motion, $\hat{v}_r\langle\hat{v}_{CM}\rangle < 0$. Vice versa, the recovery stroke is defined to be when the small sphere moves in the same direction as the net motion, $\hat{v}_r\langle\hat{v}_{CM}\rangle > 0$. In this figure, the nondimensional velocity of the spherobot, $\hat{v}_{CM}$, is represented by the purple curves. The mean swim direction $\langle\hat{v}_{CM}\rangle$ is indicated by the purple arrow in the accompanying spherobot schematics. The shaded areas under the $\hat{v}_{CM}$ curve represent the displacements: in the mean swimming direction $\Delta\hat{y}_+$ (green) and opposite to it $\Delta\hat{y}_-$ (red). The power and recovery strokes for each swimmer are labeled by *P* and *R*, respectively. (a) The spherobot in Stokes flow. Here, there is zero net displacement. Therefore, there is no power or recovery stroke observed. (b) and (c) The spherobot swims net small-sphere-leading at Re = 2.5. Its power stroke is during compression, and its recovery stroke is during expansion. (d) The spherobot does not swim and its net displacement is very small and approximated to be zero. Like Stokes flow, we do not observe a power or recovery stroke. (e) and (f) The spherobot swims large-sphere-leading at Re = 33.0 and 70.0. Its power and recovery stroke are opposite of those observed for the small-sphere-leading spherobot. The power stroke occurs during expansion, and the recovery stroke occurs during compression.

the perpendicular [see Fig. 6(c)], while in the large-sphere-leading regime the averaged flow over a cycle is pusherlike, i.e., the flow is pushed out away from the spheres along the swimming direction and is pulled in along the perpendicular; see Fig. 6(f) [39]. We related this reversal of averaged fluid flows of the spherobot to a reversal in steady streaming around a sphere calculated analytically by Riley [50]. It is noteworthy that while the spherobot operates at intermediate Reynolds numbers and the flow around it is generated by the oscillation of the spheres, its average flow field qualitatively resembles the flow around Stokesian model pullers and then pushers as Re increases and the flow field of the spherobot reverses. As discussed more by Dombrowski *et al.* [39], there is no reason to assume that such a link would exist because the source of the flow field and the hydrodynamics are different in the two cases: surface velocity oscillations at $\mathrm{Re} = 0$ in the squirmer model versus translational sphere oscillations at intermediate Re in the spherobot.

To get more insight into how the averaged fluid flow fields' reversal relates to motion, we split the flows averaging over expansion and compression separately for the two characteristic systems. The averaged flow during expansion resembles a pusher and during compression a puller for both swimming regimes. This makes intuitive sense as we expect the fluid to flow into the gap between the spheres during expansion and to be pushed out of the gap during compression. There is a competition between pusher- and puller-type flow, and depending on Re, either puller or pusher flow is more dominant, as evident by the difference in net flow fields (c) and (f).

The presence of both pullerlike and pusherlike flows during the cycle for both small-sphere leading (pullerlike overall) and large-sphere-leading (pusherlike overall) regimes is interesting because it apparently happens around living organisms, too, albeit in Stokes flows. *Chlamydomonas* and sperm cells, for example, have been shown to oscillate between puller and pusher flows even though they are classified as a puller and pusher, respectively, based on the net far field flow [66]. Relating to power and recovery strokes in each regime, it is worth noting that the flow field that occurs during the power stroke is the one that dominates over the cycle; see Fig. 6. Note that we are presenting the near-field flow here, which extends to the edge of the box $\sim 53r$. It will be interesting to do a systematic study of the near- and far-field flow and how they decay, and to compare, for example, with the fields shown by Chisholm and Khair for inertial squirmers [32].

We also calculated the efficiency of our swimmer in each regime during expansion η_{exp}, compression η_{com}, and the whole cycle η_{cyc}. We defined the efficiency to be $\eta = \Delta y_+/E$. Δy_+ is the swimmer's total distance traveled in the net swimming direction, and $E = \sum_{\tau=0}^{1} U_{\mathrm{spring}}(\tau) = \sum_{\tau=0}^{1} 0.5k[d(\tau) - x(\tau)]^2$ is the total energy added to the system over one cycle, where k is the spring constant, $d(\tau)$ is the prescribed spring length, and $x(\tau)$ is the current spring length in the simulation (see also Sec. II). There was zero contribution to the efficiency when the spherobot moved opposite to its swim direction. In Fig. 7, we calculated the efficiency of the spherobot with parameters $A = 0.18$ m and $d_0 = 0.98$ m and plotted as a function of Re. In the small-sphere-leading regime, the spherobot was more efficient during compression (Fig. 7, green dotted line) than expansion (Fig. 7, red solid line), $\eta_{\mathrm{com}} > \eta_{\mathrm{exp}}$, i.e., it was more efficient to push fluid out from between the spheres than to pull it in. In the large-sphere-leading regime, expansion (Fig. 7, green solid line) was more efficient than compression (Fig. 7, red dotted line), $\eta_{\mathrm{exp}} > \eta_{\mathrm{com}}$, i.e., it was more efficient to pull fluid in between the spheres than to push it out. For most Re, the power stroke is more efficient than the recovery stroke. However, at $\mathrm{Re} \approx 110$ for this spherobot configuration, the recovery stroke becomes more efficient than the power stroke. In fact, the Re where the recovery stroke becomes more efficient than the power stroke depends on the separation distance of the spheres, $\hat{d}_0$. The larger the separation, the larger the Re where the recovery becomes the more efficient stroke; see Fig. S11. We discuss possible explanations in the SI (Sec. III).

We can attribute the motion of the spherobot to the continuous evolution in its averaged fluid flow over a cycle (steady streaming) across Re; see Fig. 8. First, at low Re [Fig. 8(a)], the spherobot oscillations generate only one vortex layer. The flow pulls inward along the swimming axis and pushes outward along the perpendicular; see also Fig. 6(c). Because of the asymmetry in the spherobot, there is a resulting asymmetry in fluid flow. The small sphere has a larger amplitude

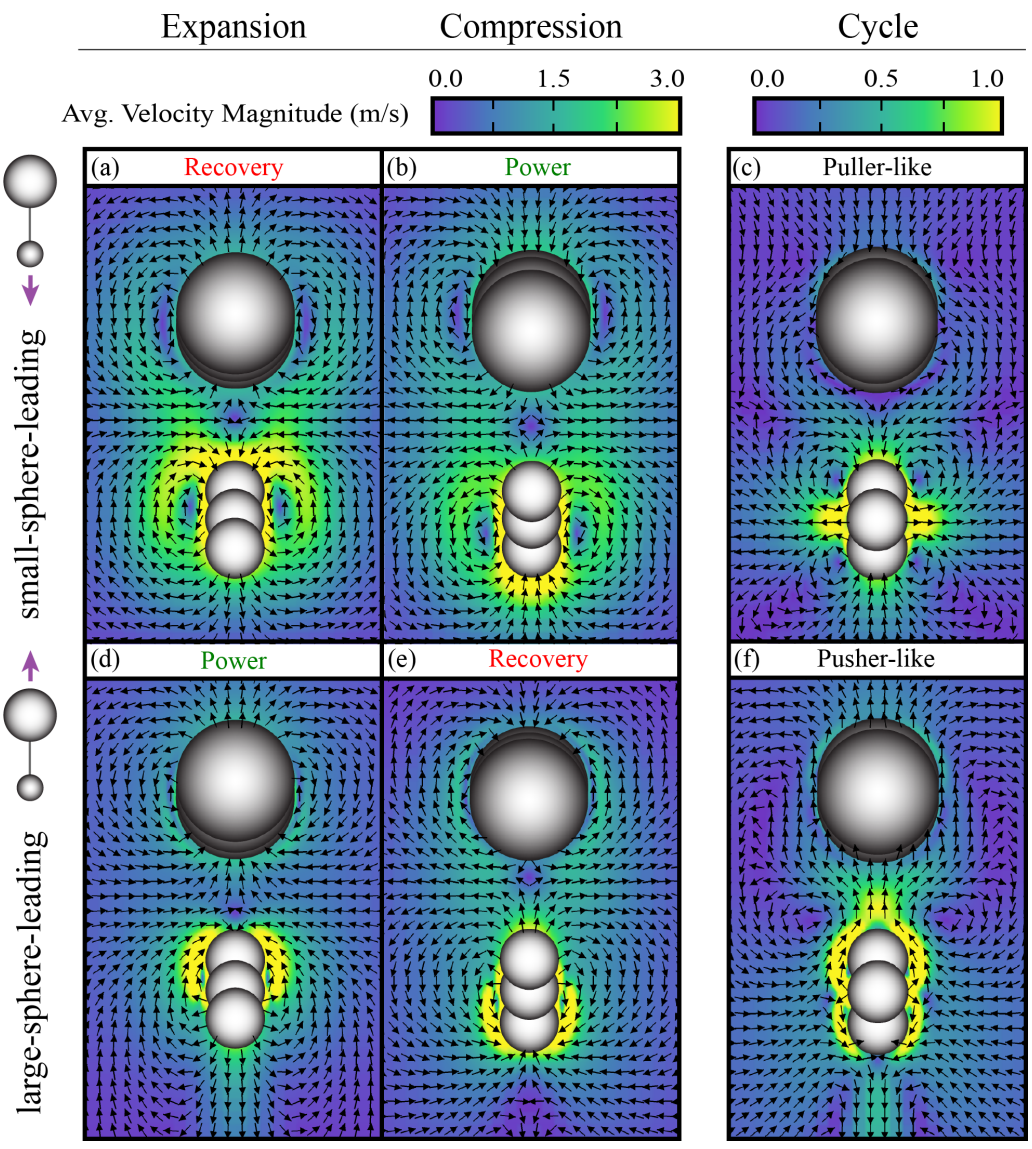

FIG. 6. The average velocity field of a small-sphere-leading (top row) and large-sphere-leading (bottom row) spherobot averaged over (left) expansion, (middle) compression, and (right) an oscillation cycle. Flow magnitudes are represented by the heat map, and the flow direction is indicated by the black arrows. (a) Flow field of small-sphere-leading spherobot averaged over expansion. The fluid flows outward along the swimming axis and inward perpendicular. (b) Flow field of small-sphere-leading spherobot averaged over compression. The flow is opposite to that of expansion, inward along the swimmer's axis and outward perpendicular. (c) Averaged over a whole cycle small-sphere-leading spherobot flow. The net flow is pullerlike. (d) Flow field of large-sphere-leading spherobot averaged over expansion. The fluid flows outward along the swimming axis and inward perpendicular. (e) Flow field of large-sphere-leading spherobot averaged over compression. The flow is opposite to that of expansion, inward along the swimmer's axis, and outward perpendicular. (f) Averaged over a whole cycle large-sphere-leading spherobot flow. The net flow is pusherlike.

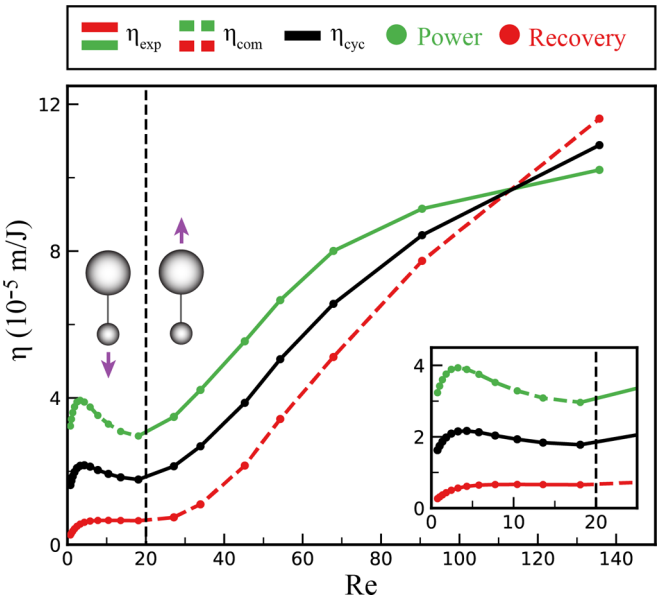

FIG. 7. Efficiency of a spherobot with parameters $\epsilon = 1.2$ and $\hat{d}_0 = 6.5$ as a function of Re where η_{exp} (solid green and red), η_{com} (dashed green and red), and η_{cyc} (black) are depicted. Also shown are the efficiencies of the power (green) and recovery (red) strokes. The inset shows a closeup of the efficiencies in the small-sphere-leading regime. Here, the power stroke occurs during compression, the recovery stroke occurs during expansion, and $\eta_{com} > \eta_{exp}$. Because there is a switch in swimming direction at Re ≈ 20, the power and recovery strokes also switch. Now, $\eta_{exp} > \eta_{com}$. As expected, the power stroke is more efficient than the recovery, but up until Re > 110 for this configuration. There is also a trend in the spherobot's cycle efficiency where swimming large-sphere-leading is generally more efficient than swimming small-sphere-leading.

so its oscillation affects the surrounding flow farther away than the large sphere does. In fact, steady streaming flows theoretically scale as $A^2\omega/\nu$ [55]. Thus the averaged flow appears to be dominated by the small sphere so much that the large sphere acts almost as an obstacle. As a result, at the lower end of Re, the spherobot moves small-sphere-leading because the fluid below the small spheres pulls it more than fluid above. As Re increases, the inner vortex layer reduces in size and extent, and eventually an additional outer vortex layer forms only below the small sphere; see Fig. 8(b). The outer vortex layer rotates counter to the inner vortex, which creates a competition between pulling the spherobot down and pushing the spherobot up along its swimming axis (stagnation point). The spherobot slows down and approaches zero. An outer vortex layer above the large sphere develops at a higher Re relative to the outer vortex below the small sphere, i.e., Fig. 8(c). When the spherobot is stationary at Re $=$ Re$_c$, the inner vortex pulls the spherobot as strongly as the outer vortex pushes it. As Re increases further, Fig. 8(d), the outer vortex above the large sphere aligns its rotation with the outer vortex above the small sphere and it disappears. The small sphere's outer vortices become more and more dominant, and the spherobot is pushed up more by the fluid below the small sphere. The inner vortex becomes smaller, $\delta = \sqrt{\nu/\omega}$, and as a result the spherobot becomes more efficient in swimming large-sphere-leading. Thus, here is another example in which we see how the spherobot's movement is due to a competition between pushing and pulling.

V. DISCUSSION

To summarize, we explored the spherobot's kinematics and its relationship with Re, amplitude ϵ, and the equilibrium distance between spheres $\hat{d}_0$ by collapsing the net displacements during

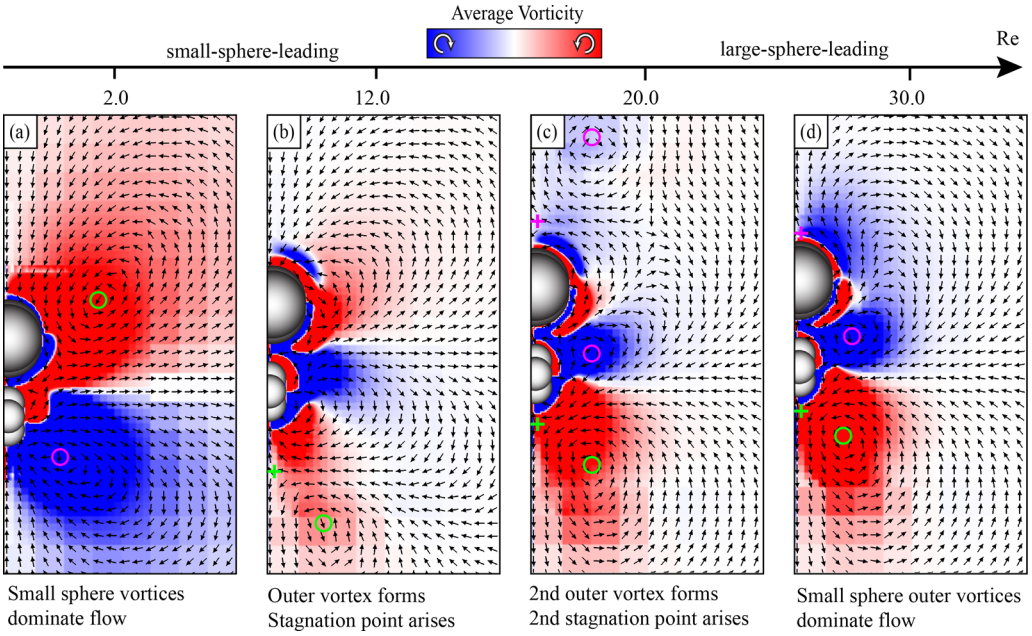

FIG. 8. The fluid flow around the spherobot continuously evolves across Re. We provide four flows averaged over a cycle, from a spherobot with $\hat{d}_0 = 5.0$ and $\epsilon = 1.2$, across both swimming regimes to highlight its evolution. Vortices of interest are identified with circles (O) and stagnation points are shown with a (+). Their colors are chosen to contrast background vorticity. (a) At Re = 2.0, the spherobot swims small-sphere-leading. We observe one pair of vortices from each sphere, and the small sphere's vortices dominate the surrounding flow. (b) At Re = 12.0, an outer vortex forms below the small sphere, which rotates counter to the inner vortex. The flow direction change below the small sphere is shown to occur at the specified stagnation point. (c) At Re = 20.0, another outer vortex forms above the large sphere with an accompanying stagnation point. There is a competition between pushing and pulling the fluid both above and below the spheres, and the spherobot does not swim. (d) The spherobot now swims large-sphere-leading at Re = 30.0. The outer vortex above the large sphere disappears, and the flow merges with the outer vortex above the small sphere, pink circle. The outer vortex below the small sphere (green circle) remains and moves closer to the spherobot. The outer vortices generated from the small sphere movement dominate the surrounding fluid flow.

expansion $\Delta\hat{y}_{\text{exp}}$ and during compression $\Delta\hat{y}_{\text{com}}$. In the small-sphere-leading regime, the spherobot performed a back-and-forth motion where it moved more in the direction of swimming during compression than in the opposite direction during expansion. The backward motion disappeared as Re increased and the spherobot moved in the direction of swimming during expansion and slowed down during compression. We categorized the spherobot's swimming into power and recovery strokes. The swim stroke itself did not change; however, due to the change in swim direction, the power and recovery strokes switched. We looked at the individual sphere's velocities and identified regions of slip where both spheres and the spherobot's CM moved in the same direction. We noticed that the slip direction at the end of the power stroke was always in the same direction as the net swimming. We analyzed the flow fields for a small-sphere-leading and large-sphere-leading spherobot. Much like living organisms, there was a competition between puller- and pusher-type flow throughout the cycle. When averaged over the whole cycle, the flow that dominated was the one that occurs during the power stroke. We calculated the efficiencies of the spherobot over the cycle as well as during expansion and compression separately. We determined that in the small-sphere-leading regime, it was more efficient to push fluid out of the gap between the spheres than to pull fluid inward; the opposite was true for most Re in the large-sphere-leading regime. There

was additional complexity in the efficiency in the large-sphere-leading regime, where we found that at high Re depending on $\hat{d}_0$ the recovery stroke was more efficient than the power stroke.

We stress the importance in understanding motility and its complexity at intermediate Re. Recent studies have reported other model swimmers that can switch their swim direction based on internal or external stimuli; see, e.g., the passively flapping plate [34] and the asymmetric dumbbell shaker [38], respectively. It remains to be seen whether other model swimmers at intermediate Re show similar behavior, and what kind of classifications can be made. The theoretical models, such as ours presented here, are important because in their simplicity they hopefully capture physical mechanisms that are obscured by complexity in studies of real organisms. For example, it is possible that steady streaming flows are present in real swimmers at intermediate Re and could explain how they swim or switch between different modes of swimming. However, few studies have investigated flow fields around intermediate-Re swimmers or even other biological systems where there are fluid oscillations at intermediate Re, e.g., in the lung [67,68].

Another area of importance is how collective behavior emerges from the nonlinearities that arise when many mesoscale organisms swim together. Are there systems where, say, two organisms individually swim in one preferred direction, but together as a collective swim differently? Finally, from an applications standpoint, it is important to understand the underlying physical mechanisms behind motility at intermediate Re, impacting the design of artificial swimmers, drones, and inertial microfluidics.

ACKNOWLEDGMENT

D.K. and T.D. acknowledge the National Science Foundation, Grant No. DMR-1753148.

[1] I. K. Bartol, P. S. Krueger, W. J. Stewart, and J. T. Thompson, Pulsed jet dynamics of squid hatchlings at intermediate Reynolds numbers, J. Exp. Biol. **212**, 1506 (2009).

[2] G. Herschlag and L. Miller, Reynolds number limits for jet propulsion: A numerical study of simplified jellyfish, J. Theor. Biol. **285**, 84 (2011).

[3] J. R. Strickler, Swimming of planktonic Cyclops species (Copepoda, Crustacea): pattern, movements and their control, in *Swimming and Flying in Nature* (Springer, Boston, MA, 1975), pp. 599–613.

[4] R. W. Blake, Hydrodynamics of swimming in the water boatman, Cenocorixa bifida, Can. J. Zool. **64**, 1606 (1986).

[5] B. J. Borrell, J. A. Goldbogen, and R. Dudley, Aquatic wing flapping at low Reynolds numbers: Swimming kinematics of the Antarctic pteropod, Clione antarctica, J. Exp. Biol. **208**, 2939 (2005).

[6] M. Mohaghar, D. Adhikari, and D. R. Webster, Characteristics of swimming shelled antarctic pteropods (limacina helicina antarctica) at intermediate Reynolds number regime, Phys. Rev. Fluids **4**, 111101 (2019).

[7] S. Kern and P. Koumoutsakos, Simulations of optimized anguilliform swimming, J. Exp. Biol. **209**, 4841 (2006).

[8] L. A. Fuiman and P. W. Webb, Ontogeny of routine swimming activity and performance in zebra danios (Teleostei: Cyprinidae), Anim. Behav. **36**, 250 (1988).

[9] J. Sznitman, X. Shen, R. Sznitman, and P. E. Arratia, Propulsive force measurements and flow behavior of undulatory swimmers at low Reynolds number, Phys. Fluids **22**, 121901 (2010).

[10] M. J. McHenry, E. Azizi, and J. A. Strother, The hydrodynamics of locomotion at intermediate Reynolds numbers: undulatory swimming in ascidian larvae (Botrylloides sp.), J. Exp. Biol. **206**, 327 (2003).

[11] A. P. S. Bhalla, B. E. Griffith, and N. A. Patankar, A forced damped oscillation framework for undulatory swimming provides new insights into how propulsion arises in active and passive swimming, PLoS Comput. Biol. **9**, e1003097 (2013).

[12] B. J. Gemmell, H. Jiang, and E. J. Buskey, A tale of the ciliate tail: Investigation into the adaptive significance of this sub-cellular structure, Proc. R. Soc. B **282**, 20150770 (2015).

[13] H. Jiang, Why does the jumping ciliate mesodinium rubrum possess an equatorially located propulsive ciliary belt? J. Plankton Res. **33**, 998 (2011).
[14] E. M. Purcell, Life at low Reynolds number, Am. J. Phys. **45**, 3 (1977).
[15] M. Lighthill, On the squirming motion of nearly spherical deformable bodies through liquids at very small reynolds numbers, Commun. Pure Appl. Math. **5**, 109 (1952).
[16] J. R. Blake, A spherical envelope approach to ciliary propulsion, J. Fluid Mech. **46**, 199 (1971).
[17] E. Lauga and T. R. Powers, The hydrodynamics of swimming microorganisms, Rep. Prog. Phys. **72**, 096601 (2009).
[18] T. J. Pedley, Spherical squirmers: Models for swimming micro-organisms, IMA J. Appl. Math. **81**, 488 (2016).
[19] G. Alexander and J. Yeomans, Dumb-bell swimmers, Europhys. Lett. **83**, 34006 (2008).
[20] E. Lauga and D. Bartolo, No many-scallop theorem: Collective locomotion of reciprocal swimmers, Phys. Rev. E **78**, 030901(R) (2008).
[21] V. B. Putz and J. Dunkel, Low reynolds number hydrodynamics of asymmetric, oscillating dumbbell pairs, Eur. Phys. J.: Spec. Top. **187**, 135 (2010).
[22] A. Najafi and R. Golestanian, Simple swimmer at low Reynolds number: Three linked spheres, Phys. Rev. E **69**, 062901 (2004).
[23] J. Avron, O. Kenneth, and D. Oaknin, Pushmepullyou: An efficient micro-swimmer, New J. Phys. **7**, 234 (2005).
[24] R. E. Goldstein, Batchelor prize lecture fluid dynamics at the scale of the cell, J. Fluid Mech. **807**, 1 (2016).
[25] S. A. Mallory, C. Valeriani, and A. Cacciuto, An active approach to colloidal self-assembly, Annu. Rev. Phys. Chem. **69**, 59 (2018).
[26] M. O. Din, T. Danino, A. Prindle, M. Skalak, J. Selimkhanov, K. Allen, E. Julio, E. Atolia, L. S. Tsimring, S. N. Bhatia *et al.*, Synchronized cycles of bacterial lysis for in vivo delivery, Nature (London) **536**, 81 (2016).
[27] E. Lauga, Continuous breakdown of purcell's scallop theorem with inertia, Phys. Fluids **19**, 061703 (2007).
[28] S. Wang and A. Ardekani, Inertial squirmer, Phys. Fluids **24**, 101902 (2012).
[29] A. S. Khair and N. G. Chisholm, Expansions at small reynolds numbers for the locomotion of a spherical squirmer, Phys. Fluids **26**, 011902 (2014).
[30] N. G. Chisholm, D. Legendre, E. Lauga, and A. S. Khair, A squirmer across reynolds numbers, J. Fluid Mech. **796**, 233 (2016).
[31] G. Li, A. Ostace, and A. M. Ardekani, Hydrodynamic interaction of swimming organisms in an inertial regime, Phys. Rev. E **94**, 053104 (2016).
[32] N. G. Chisholm and A. S. Khair, Partial drift volume due to a self-propelled swimmer, Phys. Rev. Fluids **3**, 014501 (2018).
[33] R. Mahalinkam, F. Gong, and A. S. Khair, Reduced-order model for inertial locomotion of a slender swimmer, Phys. Rev. E **97**, 043102 (2018).
[34] J. Zhang, N.-S. Liu, and X.-Y. Lu, Locomotion of a passively flapping flat plate, J. Fluid Mech. **659**, 43 (2010).
[35] S. E. Spagnolie, L. Moret, M. J. Shelley, and J. Zhang, Surprising behaviors in flapping locomotion with passive pitching, Phys. Fluids **22**, 041903 (2010).
[36] D. Klotsa, K. A. Baldwin, R. J. A. Hill, R. M. Bowley, and M. R. Swift, Propulsion of a Two-Sphere Swimmer, Phys. Rev. Lett. **115**, 248102 (2015).
[37] B. U. Felderhof, Effect of fluid inertia on the motion of a collinear swimmer, Phys. Rev. E **94**, 063114 (2016).
[38] J. F. Collis, D. Chakraborty, and J. E. Sader, Autonomous propulsion of nanorods trapped in an acoustic field, J. Fluid Mech. **825**, 29 (2017).
[39] T. Dombrowski, S. K. Jones, G. Katsikis, A. P. S. Bhalla, B. E. Griffith, and D. Klotsa, Transition in swimming direction in a model self-propelled inertial swimmer, Phys. Rev. Fluids **4**, 021101(R) (2019).

[40] T. Parthasarathy, F. K. Chan, and M. Gazzola, Streaming-enhanced flow-mediated transport, J. Fluid Mech. **878**, 647 (2019).
[41] S. Childress and R. Dudley, Transition from ciliary to flapping mode in a swimming mollusc: Flapping flight as a bifurcation in re_ω, J. Fluid Mech. **498**, 257 (2004).
[42] T. A. Williams, A model of rowing propulsion and the ontogeny of locomotion in artemia larvae, Biol. Bull. **187**, 164 (1994).
[43] A. T. Sensenig, K. T. Kiger, and J. W. Shultz, The rowing-to-flapping transition: ontogenetic changes in gill-plate kinematics in the nymphal mayfly centroptilum triangulifer (ephemeroptera, baetidae), Biol. J. Linn. Soc. **98**, 540 (2009).
[44] D. Klotsa, As above, so below, and also in between: Mesoscale active matter in fluids, Soft Matter **15**, 8946 (2019).
[45] See Supplemental Material at http://link.aps.org/supplemental/10.1103/PhysRevFluids.5.063103 for more details on methods, additional figures and movies of the spherobot.
[46] B. Kallemov, A. P. S. Bhalla, B. E. Griffith, and A. Donev, An immersed boundary method for rigid bodies, Commum. Appl. Math. Comput. Sci. **11**, 79 (2016).
[47] F. Balboa Usabiaga, B. Kallemov, B. Delmotte, A. P. S. Bhalla, B. E. Griffith, and A. Donev, Hydrodynamics of suspensions of passive and active rigid particles: A rigid multiblob approach, Commun. Appl. Math. Comput. Sci. **11**, 217 (2016).
[48] B. E. Griffith, R. D. Hornung, D. M. McQueen, and C. S. Peskin, An adaptive, formally second order accurate version of the immersed boundary method, J. Comput. Phys. **223**, 10 (2007).
[49] IBAMR: An adaptive and distributed-memory parallel implementation of the immersed boundary method, https://github.com/IBAMR/IBAMR.
[50] N. Riley, On a sphere oscillating in a viscous fluid, Q. J. Mech. Appl. Math. **XIX**, 461 (1966).
[51] N. Vandenberghe, S. Childress, and J. Zhang, On unidirectional flight of a free flapping wing, Phys. Fluids **18**, 014102 (2006).
[52] N. Vandenberghe, J. Zhang, and S. Childress, Symmetry breaking leads to forward flapping flight, J. Fluid Mech. **506**, 147 (2004).
[53] S. Alben and M. Shelley, Coherent locomotion as an attracting state for a free flapping body, Proc. Natl. Acad. Sci. (USA) **102**, 11163 (2005).
[54] H. Schlichting and K. Gersten, *Boundary-layer Theory* (Springer, Berlin, Heidelberg, 2017).
[55] N. Riley, Steady streaming, Annu. Rev. Fluid Mech. **33**, 43 (2001).
[56] E. J. Chang and M. R. Maxey, Unsteady flow about a sphere at low to moderate reynolds number. part 1. oscillatory motion, J. Fluid Mech. **277**, 347 (1994).
[57] W. Coenen, Steady streaming around a cylinder pair, Proc. R. Soc. London, Ser. A **472**, 20160522 (2016).
[58] M. Tatsuno, Secondary flow induced by a circular cylinder performing unharmonic oscillations, J. Phys. Soc. Jpn. **50**, 330 (1981).
[59] C. W. Kotas, M. Yoda, and P. H. Rogers, Visualization of steady streaming near oscillating spheroids, Exp. Fluids **42**, 111 (2007).
[60] D. Klotsa, M. R. Swift, R. M. Bowley, and P. J. King, Interaction of spheres in oscillatory fluid flows, Phys. Rev. E **76**, 056314 (2007).
[61] D. Klotsa, M. R. Swift, R. M. Bowley, and P. J. King, Chain formation of spheres in oscillatory fluid flows, Phys. Rev. E **79**, 021302 (2009).
[62] H. Childs, E. Brugger, B. Whitlock, J. Meredith, S. Ahern, D. Pugmire, K. Biagas, M. Miller, C. Harrison, G. H. Weber, H. Krishnan, T. Fogal, A. Sanderson, C. Garth, E. W. Bethel, D. Camp, O. Rübel, M. Durant, J. M. Favre, and P. Navrátil, VisIt: An End-User Tool For Visualizing and Analyzing Very Large Data, in *High Performance Visualization–Enabling Extreme-Scale Scientific Insight* (2012), pp. 357–372, https://wci.llnl.gov/simulation/computer-codes/visit/faqs/faq09.
[63] S. Vogel, *Life's Devices* (Princeton University Press, Princeton, NJ, 1988).
[64] F. E. Fish, Transitions from drag-based to lift-based propulsion in mammalian swimming, Am. Zool. **36**, 628 (1996).
[65] S. Alben, L. Miller, and J. Peng, Efficient kinematics for jet-propelled swimming, J. Fluid Mech. **733**, 100 (2013).

[66] G. S. Klindt and B. M. Friedrich, Flagellar swimmers oscillate between pusher- and puller-type swimming, Phys. Rev. E **92**, 063019 (2015).
[67] H. Kumar, M. H. Tawhai, E. A. Hoffman, and C.-L. Lin, Steady streaming: A key mixing mechanism in low-reynolds-number acinar flows, Phys. Fluids **23**, 041902 (2011).
[68] J. B. Grotberg, Respiratory fluid mechanics, Phys. Fluids **23**, 021301 (2011).